Turbulent Flow in Supersonic and Hypersonic Nozzles

Jiasen Hu* and Arthur Rizzi†

Royal Institute of Technology, S-100 44 Stockholm, Sweden

The calculated turbulent flow properties in a supersonic or a hypersonic wind-tunnel nozzle are affected by the location of laminar-turbulent transition point and the behavior of the particular turbulence models considered. These effects are studied numerically by solving Reynolds-averaged Navier–Stokes equations for two nozzles. Results are reported using either an algebraic turbulence model or two alternative k–ϵ models in which one contains two kinds of explicit compressibility corrections. The numerical method is based on a finite volume technique using a space centered Runge–Kutta scheme which is explicit to the mean flow equations and semi-implicit to the k and ϵ equations. These calculations provide us a better understanding of the mechanism controlling this kind of flowfield. It is found that a small variation of transition point in near throat region has substantial global effects on the computed results downstream. Including explicit compressibility corrections in modeling the hypersonic nozzle flow introduces nonnegligible effects into the solution and improves its accuracy. The turbulence transport effects are also demonstrated.

Nomenclature

c_f	= local skin friction coefficient
$c_\mu, c_1, c_2, c_3, c_{p1}$	= constants in k–ϵ models
E	= energy per unit mass
$\bar{F}_I, \bar{F}_V$	= inviscid and viscous flux tensor
f_μ, f_2	= damping functions in k–ϵ models
H	= stagnation enthalpy, $E + p/\rho$
$\bar{I}$	= unit tensor
k	= turbulent kinetic energy
k^+	= normalized k, $\sqrt{k}/V_c$
M	= Mach number
m^+	= normalized mass flow, $\rho V/(\rho V)_c$
n	= normal distance from wall
n^+	= wall coordinate, $\rho u_\tau n/\mu$
P_k	= production of k
p	= pressure
Q	= conservative variable vector
q	= conductive heat flux
r	= nozzle radius
St	= Stanton number
T	= temperature
V	= magnitude of v
v	= velocity
x, y	= Cartesian coordinates
γ	= specific heat ratio
δ^*	= boundary-layer displacement thickness
ϵ	= dissipation rate of k
μ	= viscosity
ρ	= density
$\sigma_k, \sigma_\epsilon, \sigma_\rho$	= turbulent Prandtl numbers
$\bar{\tau}$	= stress tensor
$\omega_k, \omega_\epsilon$	= turbulent source terms

Subscripts

c	= centerline
l	= laminar
t	= turbulent
tp	= transition point
w	= wall
0	= stagnation

Superscripts

$\prime$	= fluctuating quantity in Reynolds averaging
$\prime\prime$	= fluctuating quantity in Favre averaging
$-$	= Reynolds-averaged quantity

Introduction

RECENT interest in hypersonic vehicles has reactivated numerical studies in various nozzle flows for the purpose of developing new wind-tunnel nozzles, propulsive nozzles, exhaust nozzles, etc. The mechanisms of high-speed flows, however, have complex features due to the variations in density and temperature, among others. Therefore, even for calculating nonchemical reaction turbulent boundary layers in high-speed wind-tunnel nozzles, some previous investigations (for example, see Refs. 1 and 2) have shown that there still exist some deficiencies in the calculated results. One of the reasons for the deficiencies could be due to the uncertainties stemming from the treatment of the laminar-turbulent transition point and the compressible turbulence modeling.

The air flow in a convergent-divergent wind-tunnel nozzle starts from a stagnation state in a reservoir and transits sequentially from static, subsonic, and transonic to supersonic or further to hypersonic. The Reynolds number increases in the streamwise direction and the boundary layer undergoes laminar-turbulent transition at a certain location. For practical wind-tunnel nozzles, however, it is usually impossible to get knowledge of this location experimentally. A common simplification of this problem at present, in engineering applications, is then to locate the transition point by some more or less empirical approaches, but it obviously induces unavoidable error in the specified transition locations. The first objective of this work is, then, to calibrate the sensitivity of the computed results to the aforementioned error. To simplify the problem, that error is modeled by a small variation in the location of the transition point. Calculations are then performed with different transition points specified, and the purpose is achieved by examining the resulting differences among the solutions.

The second objective of the paper is to investigate the importance of explicit compressibility corrections in turbulent nozzle simulations. This is related to the problem of high-speed turbulence modeling. Traditionally, models proposed originally for incompressible flows have been applied to compressible conditions with little or no modification when Favre (mass-weighted) averaging is considered, namely, the variable density extension of incompressible models according to Morkovin's hypothesis.[3] It is generally believed that this approach works for flows with moderate density fluctuations, for instance, turbulent boundary layers with freestream Mach number $M < 5$ and jets with $M < 1.5$ (Ref. 4). Since the fluctuations in thermodynamic variables become progressively more important

*Graduate Student, Aeronautical Engineering Division.
†Professor, Aeronautical Engineering Division. Senior Member AIAA.

when the Mach number of a turbulent flow increases, however, the ability of those standard models, i.e., the models constructed on the basis of Morkovin's hypothesis, to reliably predict compressible turbulent flows at higher Mach numbers has been called into question.[5] Accordingly, some investigators have tested the explicit compressibility modifications in several kinds of high-speed turbulent cases, including mixing layer, flat-plate boundary layer, flow over ramp and over backward facing step, etc. (see, for example, Refs. 6–8). In the present work, we will explore how the compressibility corrections behave in a different situation, i.e., the hypersonic wind-tunnel nozzle flows.

The last objective of the paper is to show the transport effects on hypersonic turbulent wind-tunnel nozzle simulations. Accordingly, we use both the Baldwin–Lomax turbulence model[9] and a k–ϵ model[10] to do the calculations whereas, to our knowledge, only algebraic models were previously adopted in such computations.[1,2,11]

In the literature, the existing publications on wind–tunnel nozzle flows, especially the low-enthalpy hypersonic case, are relatively few, and among those low-enthalpy computations reported,[1,2,11] no investigations of a nature similar to ours were carried out. Therefore, the influence of turbulence transport, explicit compressibility, and transition location on the computed nozzle results is still poorly understood and, hence, requires investigations.

In this work we consider two nozzles that are in the perfect gas regime and have relatively high Reynolds numbers. The first is a M4 supersonic nozzle with an exit area ratio of 11.8 over a 3.32 m length. The other is a M7 hypersonic nozzle whose exit area ratio is 138.9 over a 3.31 m length. They are both axisymmetric contoured nozzles used in a classical low-enthalpy hypersonic wind tunnel, called HYP 500, at the Aeronautical Research Institute of Sweden, FFA. Their shapes are shown in Fig. 1 with the coordinate system used in the present work. Additional characterization of the facility can be found in Ref. 12.

Numerical Method

The computations were carried out by solving three-dimensional Reynolds-averaged Navier–Stokes equations. If written in integral form over a control volume Ω with the boundary $\partial\Omega$ and the outer normal unit vector n, the system reads

$$\frac{\partial}{\partial t} \int\int\int_{\Omega} Q \, d\Omega + \int\int_{\partial\Omega} \bar{\bar{F}}(Q) \cdot n \, dS = 0 \tag{1}$$

where $Q = [\rho, \rho v, \rho E]^T$ and flux tensor $\bar{\bar{F}}$ is composed of inviscid and viscous parts as $\bar{\bar{F}} = \bar{\bar{F}}_I - \bar{\bar{F}}_V$ with

$$\bar{\bar{F}}_I = \begin{pmatrix} \rho v \\ \rho vv + p\bar{\bar{I}} \\ \rho Hv \end{pmatrix}, \qquad \bar{\bar{F}}_V = \begin{pmatrix} 0 \\ \bar{\bar{\tau}} \\ v \cdot \bar{\bar{\tau}} - q \end{pmatrix} \tag{2}$$

In Eq. (2), $\bar{\bar{\tau}}$ and q are total stress tensor and total heat flux vector, respectively, given by $\bar{\bar{\tau}} = \bar{\bar{\tau}}_l + \bar{\bar{\tau}}_t$ and $q = q_l + q_t$. All of the primitive variables in the system are mean quantities. The air is assumed to be a perfect gas. The laminar viscous terms are stated by Fourier's law, Newton's law, and Stokes' hypothesis. The turbulent viscous terms are closed by three alternative eddy-viscosity turbulence models.

Turbulence Models

The first turbulence model used in this work is the two-layer algebraic model of Baldwin and Lomax.[9] In this model, turbulence of the inner region is based on the Prandtl mixing length theory with the improvement of the Van Driest formulation. Outer turbulence is modeled by the Clauser formulation using Klebanoff approximation of the Gaussian error function that gives the intermittency factor. The empirical constants involved are set to their standard values found in Ref. 9.

The second model is the low-Reynolds-number k–ϵ model of Chien.[10] It is a standard two-equation closure based on the following

modeled k and ϵ transport equations and without compressibility corrections beyond the Morkovin's hypothesis:

$$\frac{\partial(\rho k)}{\partial t} + \nabla \cdot (\rho k v) - \nabla \cdot \left[\left(\mu_l + \frac{\mu_t}{\sigma_k}\right)\nabla k\right] = \omega_k \tag{3}$$

$$\frac{\partial(\rho \epsilon)}{\partial t} + \nabla \cdot (\rho \epsilon v) - \nabla \cdot \left[\left(\mu_l + \frac{\mu_t}{\sigma_\epsilon}\right)\nabla \epsilon\right] = \omega_\epsilon \tag{4}$$

The turbulent viscosity is obtained from $\mu_t = c_\mu f_\mu \rho k^2/\epsilon$. The two turbulent source terms are given by

$$\omega_k = P_k - \rho\epsilon - 2\mu_l k/n^2 \tag{5}$$

$$\omega_\epsilon = c_1(\epsilon/k)P_k - c_2 f_2 \rho(\epsilon^2/k) - \left(2\mu_l\epsilon/n^2\right)\exp(-0.5\,n^+) \tag{6}$$

where $P_k = (\bar{\bar{\tau}}_t \cdot \nabla) \cdot v$. The constants are set to their standard values: $c_\mu = 0.09, c_1 = 1.35, c_2 = 1.8, \sigma_k = 1.0$, and $\sigma_\epsilon = 1.3$. This model is called Chien model in the paper and denoted by CH for convenience.

The third model is the Chien model containing two compressibility corrections in ω_k and ω_ϵ.

The first correction comes from the pressure gradient-velocity term $\overline{v''} \cdot \nabla p$ which appears in the exact k equation.[13] This term vanishes in incompressible condition and, hence, represents a kind of explicit compressibility effect as well as the influence of mean flow pressure gradients. Considering the physical characteristics of the flowfield, taking $\overline{v''} \cdot \nabla p$ into account is believed to be necessary. Since $\overline{v''}$ is related to the turbulent mass flux $\overline{\rho'v'}$ by $\overline{v''} = -\overline{\rho'v'}/\rho$, and this flux can be approximated with the standard gradient transport hypothesis as $\overline{\rho'v'} = -\mu_t\nabla\rho/\rho\sigma_\rho$, the modeled pressure gradient-velocity term is then obtained:

$$\overline{v''} \cdot \nabla p = \left(\mu_t/\rho^2\sigma_\rho\right)\nabla\rho \cdot \nabla p \tag{7}$$

The other correction is due to the compressible dissipation,[14,15] which has been found to be increasingly important in hypersonic turbulent boundary layers as Mach number and wall cooling increase.[8] To account for this extra compressible mechanism, we use the Nichols model[6] to modify the P_k term in the k equation

$$P_{k(\text{modified})} = P_k - c_{p1}(\gamma - 1)MM_t^2 P_k \tag{8}$$

Since this model includes the effects of both the turbulent Mach number M_t and mean flow Mach number M, it could be more suitable for the nozzle flow simulations performed than some other compressible dissipation corrections.

After absorbing the two corrections given in Eqs. (7) and (8), the turbulent source terms are modified to

$$\omega_k = \left[1 - c_{p1}(\gamma - 1)MM_t^2\right]P_k - \rho\epsilon - \left(\mu_t/\rho^2\sigma_\rho\right)\nabla\rho \cdot \nabla p$$
$$- 2\mu_l k/n^2 \tag{9}$$

$$\omega_\epsilon = c_1(\epsilon/k)P_k - c_2 f_2\rho(\epsilon^2/k) - c_3\left(\mu_t/\rho^2\sigma_\rho\right)(\epsilon/k)\nabla\rho \cdot \nabla p$$
$$- \left(2\mu_l\epsilon/n^2\right)\exp(-0.5\,n^+) \tag{10}$$

where $c_{p1} = 4.0, c_3 = 2.0$, and $\sigma_\rho = 0.5$.

The Chien model with the modified ω_k and ω_ϵ given in Eqs. (9) and (10) will be called the corrected Chien model hereafter and denoted by CH(corr) for convenience.

Scheme and Algorithm

The governing equations have been solved by a general purpose three-dimensional multiblock/multigrid code EURANUS.[16] The algorithm is based on a cell-centered finite volume approximation using structured meshes in Cartesian coordinates. The numerical inviscid flux at a cell face is computed via the central interpolation with a scalar artificial viscosity being added to stabilize this discretization. The viscous and turbulent production terms are computed by a cell-vertex scheme using an auxiliary staggered grid with

the gradient theorem applied. The resulting semidiscrete system is integrated to the steady state by a four-stage explicit Runge–Kutta scheme, whereas the stiffness introduced by the k–ϵ models is counteracted by a semi-implicit treatment.[13] The iteration is accelerated by means of local time stepping and implicit residual smoothing. Additionally, a standard V-cycle multigrid method is applied to the Baldwin–Lomax calculations. More details about the scheme can be found in other publications[16,17] and in our original report.[18]

Numerical Calculation

To calibrate the sensitivity of the results to the transition location, the transition is assumed to occur instantaneously at two different positions within the nozzles, which are indicated by TP1 and TP2, respectively, in Fig. 1. The first position, TP1, is at the throat of each nozzle and consistent with the choice made by some other investigators.[1,2] The TP2 is set downstream TP1 approximately by 10% the length of the divergent section of the M7 nozzle.

Five cases are studied in the present work and listed in Table 1. The numerical results are compared with the boundary-layer properties measured at the nozzle exits by Hovstadius[19] with a mass-flow probe system. The temperatures were varying along the wall, due to the cooling of the nozzle throat regions, but no precise data of the wall temperatures were reported in Ref. 19; thus an isothermal wall condition is adopted as an adequate simplification for the numerical computations.[1] Since we have no other precise information to base it on, the particular T_w set for each nozzle case is the design wall temperature at each exit, which presumably is the averaged maximum expected for the temperature at this location. Other flow conditions, p_0 and T_0, are the same as reported in the experiments, and given in Table 2 together with the specified wall temperatures and the Reynolds numbers which are based on the distance from the sonic throat to the test station.

The turbulent flows have been simulated from the TP1 or TP2 section to the exit of the nozzles. A laminar solution was calculated first in the region from a position upstream TP1 to the corresponding transition location in each case, setting up reasonable laminar boundary-

layer profiles there. The inflow boundary of this laminar region is chosen at the cross section where $M_c = 0.5$ in all of the cases.

The computational domain is taken as half of the symmetry plane with a small sector in the spanwise direction since the flow is axisymmetric. A grid resolution study was performed on part of each domain, leading to the final grid size for the whole domain with 798×128 cells for the M4 nozzle and 600×116 cells for the M7 nozzle, respectively. In these final grid systems, the first nodes next to the nozzle walls are well located in the viscous sublayer. Specifically, the n^+ value of this node at the exit of the M4 nozzle is approximately equal to 1, and less than 1 for the M7 nozzle. At both exits, about 100 cells are inside the experimentally measured boundary layers and at least 14 cells are in the range of $n^+ \leq 20$. In streamwise direction each of the meshes is clustered near the nozzle throat in order to capture correctly the sharp flow gradients in that region and keep the maximum cell aspect ratio at a suitable level.

Boundary Conditions

In the current nozzle calculations we have five different types of boundaries: 1) inlet, 2) transition section, 3) solid wall, 4) outlet, and 5) centerline. According to the theory of characteristics, the flow angles, total pressure, total temperature, and isentropic relations are used at the inlet to give subsonic boundary conditions there. At the transition section, the boundary conditions for mean flow variables are determined via the appropriate Riemann invariants. The conditions for k and ϵ are approximated by the following empirical expressions, $k_{tp} = 1.5(Tu)^2(v_{tp} \cdot v_{tp})$ and $\epsilon_{tp} = c_\mu^{3/4} k_{tp}^{3/2}/l_{tp}$. The turbulence intensity, $Tu = 0.1\%$ and length scale, $l_{tp} = 0.09\delta$ (δ is the local laminar boundary-layer thickness) are used here. On nozzle wall the no-slip condition and corresponding T_w are specified, whereas k_w and ϵ_w are set to zero. The normal pressure gradient is supposed to be zero, giving the wall pressure. At the outlet boundary, all of the flow variables are extrapolated. Symmetry conditions are applied at the nozzle centerline boundary.

Results and Discussion

The computed results are presented in this section and compared with the experimental data from Ref. 19. To be consistent with the measurements, the velocity, temperature, and mass flow profiles are normalized by the local centerline values. It should be mentioned that because the available data are not complete and our main purpose at this stage, as stated in the introductory section, is to verify the importance of the three issues, namely, the transition location effects, explicit compressibility effects, and transport effects, on the nozzle cases selected here, we do not carry out an exhaustive accuracy study of each model for each case in this work.

M4 Nozzle Case

The Mach number isolines obtained from the M4 case (case 1) are shown in Fig. 2, which gives us an overall demonstration of the flowfield within this supersonic nozzle. It is seen that an attached boundary layer is developing along the wall and the calculated nonuniformity in the exit Mach number is less than 0.04.

The detailed Mach number, velocity, temperature, and mass flow profiles at the measuring station are given in Fig. 3, where the boundary layer extends to about 20% of the local radius. In comparison with the experiments, the Mach number, velocity, and mass flow profiles are in very good agreement. But some deviations exist between the computed temperature profile and data in the near-wall region. Keep in mind that the temperature in the experiments was not measured directly and underwent more data reductions with more parameters involved than the other quantities presented[19,20]; thus, these data contain more uncertainty, especially in the near-wall region. This experimental uncertainty and the neglect of the wall temperature history by specifying a constant T_w can be the reasons for the deficiencies observed. However, the temperature profile agrees well with the data in the outer region of the boundary layer.

Table 1   Definition of computed cases

Case	Nozzle	Transition point	Turbulence model
1	M4	TP1	Baldwin–Lomax
2	M7	TP1	Baldwin–Lomax
3	M7	TP1	Chien
4	M7	TP2	Chien
5	M7	TP1	Corrected Chien

Table 2   Flow conditions

Nozzle	p_0, Pa	T_0, K	T_w, K	Re
M4	1.2×10^6	450	343	0.9×10^8
M7	1.0×10^7	580	353	1.4×10^8

Fig. 1   Nozzle contours: a) M4 and b) M7.

Fig. 2   Mach number isolines, $\Delta M = 0.04$, in M4 nozzle, case 1.
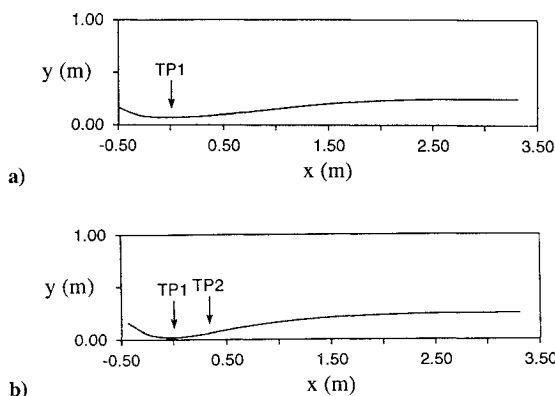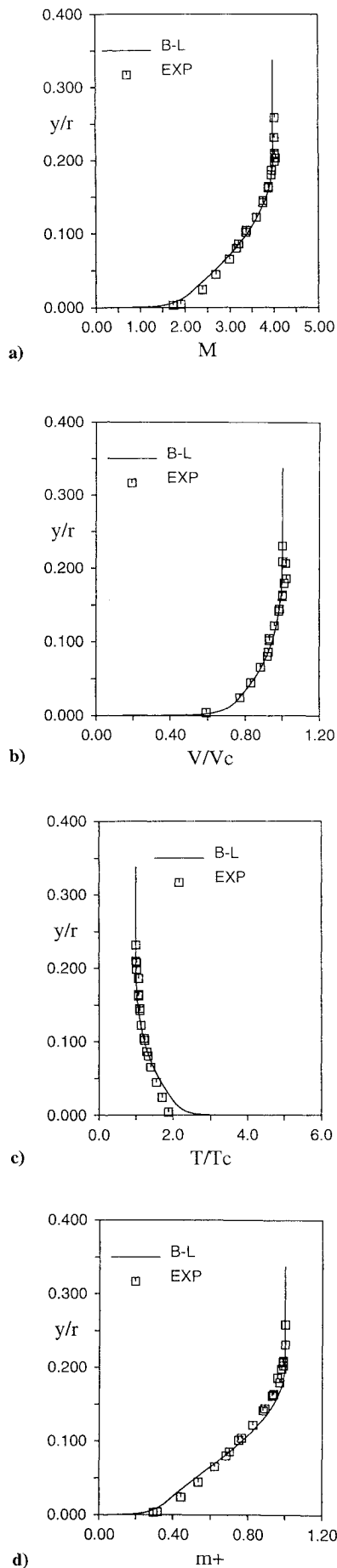
a)

b)

c)

d)

Fig. 3 Radial profiles at M4 nozzle exit, case 1 compared with experiments: a) Mach number, b) velocity, c) temperature, and d) mass flow.

Table 3 Errors of computations compared with experiments at M7 nozzle exit

Error	Case 2,%	Case 3, %	Case 4, %	Case 5, %
M_c	−2.8	−1.9	−0.7	−1.4
δ^*	18.4	8.0	−12.3	−0.5
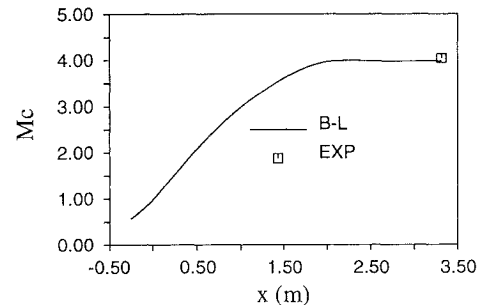
Fig. 4 Centerline Mach numbers for M4 nozzle, case 1 compared with experiment.
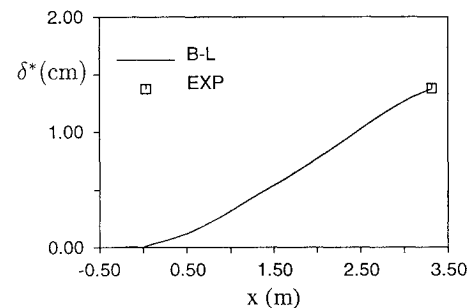
Fig. 5 Boundary-layer displacement thickness for M4 nozzle, case 1 compared with experiment.

Presented in Figs. 4 and 5 are the distributions of local centerline Mach number and boundary-layer displacement thickness from case 1. At the nozzle exit the computed $M_c = 3.978$ and $\delta^* = 1.374$ cm whereas the data are 4.04 and 1.38 cm, respectively, giving a relative error of −1.5% to M_c and −0.4% to δ^*.

Since the standard Baldwin–Lomax model in this case generally produces good results in comparison with the experimental data, this means that it is appropriate to simulate supersonic turbulent wind-tunnel nozzle flows investigated in this study, and modeling the turbulence transport is probably not necessary from the computational point of view.

M7 Nozzle Cases

The Mach number isolines from all of the M7 calculations (cases 2–5) are presented in Fig. 6 where the shapes of the contours are almost same as each other. As seen from the figure, the contours depart from radial uniformity when the flow accelerates rapidly in the nozzle expansion region. Farther downstream the uniformity gradually recovers, giving the calculated exit Mach number a nonuniformity about 0.1 in all of the cases. The development of an attached boundary layer is clear.

To show the details of the flowfield, the mean flow profiles at the exit section are presented in Fig. 7, whereas Fig. 8 gives the corresponding radial and near-wall distributions of k^+. Shown in Figs. 9–13 are the resulting axial profiles of M_c, δ^*, c_f, St, and $\log(p_w/p_0)$, respectively. Notice that the differences among the results obtained in different M7 cases can be distinguished from these figures, which clearly reveal the effects of varying transition point and modeling explicit compressibility and turbulence transport. More details will be discussed subsequently.

To verify the accuracy of the results, Table 3 gives the relative errors of the calculated M_c and δ^*, in comparison with the experimental data, at the nozzle exit for all of the M7 cases.
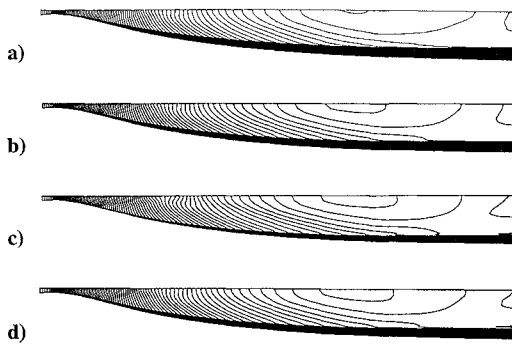
Fig. 6 Mach number isolines, $\Delta M = 0.07$, in M7 nozzle: a) case 2, Baldwin–Lomax, TP1, b) case 3, CH, TP1, c) case 4, CH, TP2, and d) case 5, CH(corr), TP1.

Baldwin–Lomax Solution

For the M7 hypersonic nozzle, a test case using the standard Baldwin–Lomax model with the transition at the throat, i.e., case 2, was calculated first to see whether this approach can also give satisfactory results as it does in the M4 case. As seen from Table 3 and Fig. 7, however, the results here are obviously less accurate, compared to the experiments, than those obtained in case 1. Table 3 shows that the computed δ^* is overpredicted with an error over 18%. In Fig. 7 only the velocity profile is adequately obtained, whereas the others are predicted to be somewhat thicker than the measured. But as pointed by Hopkins and Keener,[1] this good agreement in the velocity profile can be a result of compensating effects from the underpredicted Mach number and overpredicted temperature inside the boundary layer since $V \propto MT^{1/2}$.

In contrast with the supersonic case, therefore, case 2 shows that the standard Baldwin–Lomax model behaves less satisfactorily in the hypersonic nozzle condition. This indicates that not only the turbulence diffusivity but also the contributions from compressibility, transport, and pressure gradient should be considered in a hypersonic flow environment because they are stronger than those are in a supersonic case.

Transport Effects

As expected, the transport mechanism introduces some significant effects on the computed hypersonic results. By examining the results of case 2 and case 3 in Fig. 7, it is seen that all of the mean flow profiles obtained in case 3 are getting thinner beyond the wall region due to the influence of the turbulent history upstream.[21] In Figs. 10–12 the resulting δ^*, c_f, and St profiles in these two cases also show considerable differences. At the nozzle exit section, for instance, a 9.6% decrease in δ^*, a 1.8% decrease in c_f, and a 35.6% increase in St have been found in case 3 due to the inclusion of the transport mechanism by the Chien model. However, the computed M_c and p_w are much less affected, as seen from Figs. 9 and 13.

Comparing the results of case 3 with the experiments, Fig. 7 shows that the Mach number profile has a good agreement with the data, and the distributions of temperature and mass flow are improved except for the velocity profile which has some departure from the measurements. Additionally, Table 3 shows that the calculated M_c and δ^* at the exit are closer to the data than those from the Baldwin–Lomax solution. Therefore, including the transport mechanism in simulating this kind of hypersonic nozzle flows has proved to have some important effects on the results, and generally leads to improved comparison to experimental measurements.

Effects of Varying Transition Point

As the distance between TP1 and TP2 is small, one would anticipate that moving the transition point in the near throat region would have only local effects on the solution. But the results from case 3 and case 4 show that this variation actually has substantial global effects on the flowfield downstream. Shown in Fig. 7, the mean flow boundary-layer profiles in case 4 become obviously thinner in the outer region because the variation changes the turbulence structure upstream of the position in question. These changes in the mean
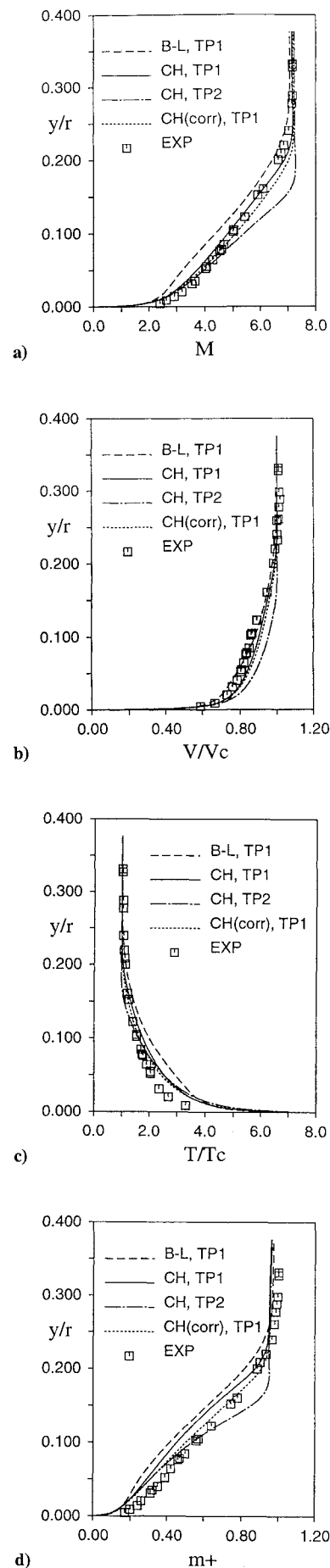

Fig. 7 Radial profiles at M7 nozzle exit, cases 2–5 compared with experiments: a) Mach number, b) velocity, c) temperature, and d) mass flow.
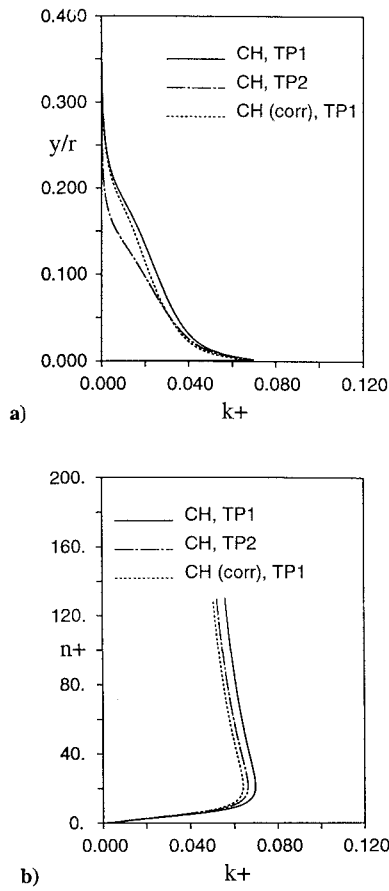
Fig. 8 Turbulent kinetic energy levels at M7 nozzle exit, cases 3–5:
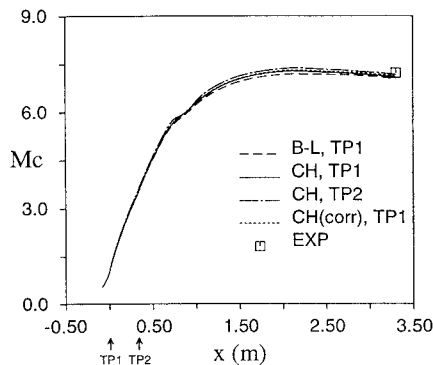a) radial profiles and b) near-wall variations.

Fig. 9 Centerline Mach numbers for M7 nozzle, cases 2–5 compared to experiment.
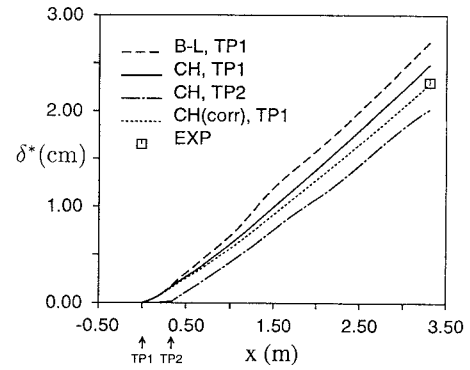

Fig. 10 Boundary-layer displacement thickness for M7 nozzle, cases 2–5 compared to experiment.
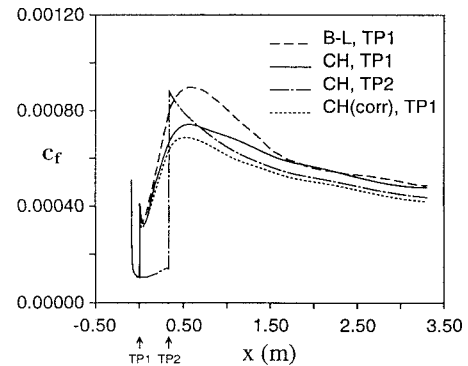

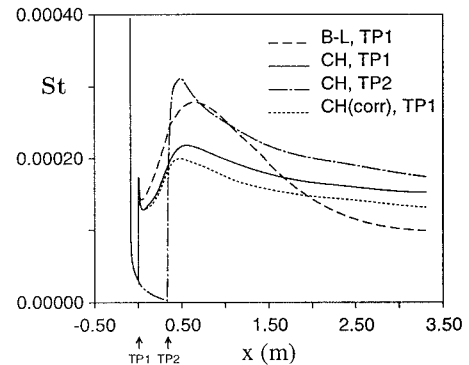Fig. 11 Local skin friction coefficients for M7 nozzle, cases 2–5.

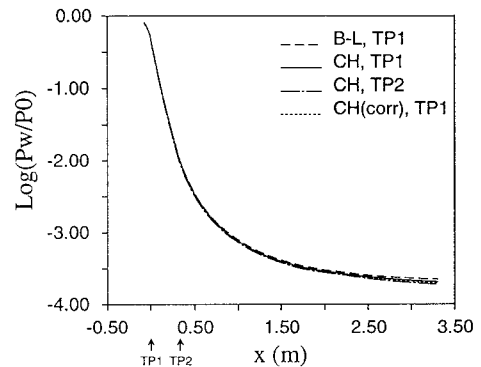Fig. 12 Stanton number distributions for M7 nozzle, cases 2–5.

Fig. 13 Wall pressure distributions for M7 nozzle, cases 2–5.

flow profiles agree well with a reduced turbulence level obtained in case 4 (Fig. 8).

As seen from Figs. 10–12, the computed values of δ^*, c_f, and St are quite sensitive to the variation. At the nozzle exit the predicted δ^* decreases by 18.8% due to the transition point moving from TP1 to TP2. The c_f decreases by 8.7% whereas the St increases by 14.2%, respectively. On the other hand, the centerline Mach number (Fig. 9) and the wall pressure (Fig. 13) are both basically unaffected by this variation.

In Fig. 8b, the maximum value of k^+ occurs around $n^+ = 20 \sim 25$, which corresponds to the location of maximum production of k. The values of this n^+ position obtained in case 3 and case 4 are essentially identical, meaning that this position is insensitive to the location of transition point upstream.

Compared to case 3, more deviations from the measurements appear in the results of case 4 except for a slight improvement in the centerline Mach number obtained. This means that TP1 is much closer to the physical location of the transition point than TP2.

Explicit Compressibility Effects

Effects of the introduced explicit compressibility corrections are revealed by comparing the results from cases 3 and 5. Shown in Fig. 7, the corrected Chien model produces a fuller Mach number and velocity profile in the boundary layer. Compared to the case of Chien model, the mass flow increases and the temperature decreases. These features are in good agreement with the predicted reduction of the turbulence level shown in Fig. 8 and in accordance with the

favorable pressure gradient existing inside the boundary layer. It should be noted, however, that the resulting substantial differences between the computed mean flow profiles are mainly found in the outer region of the boundary layer.

As shown in Figs. 10–12, the two models lead to a similar pattern for each distribution of δ^*, c_f, and St, but differences between the two cases are visible. It is seen that the corrected Chien model reduces all of these three quantities. Specifically, the exit δ^*, c_f, and St decrease by 7.9%, 12.2%, and 13.6%, respectively, due to the modeling of the explicit compressibility. For the c_f and St profiles the resulting differences increase gradually from TP1 to a certain place in the nozzle expansion region, after which the differences remain approximately constant. This phenomenon agrees with the variations in the M_c profiles. As shown in Figs. 9 and 13, however, the effects of the compressibility modifications on the predicted centerline Mach number and wall pressure are very small, and they are also not very significant on the computed n^+ position representing the location of maximum value of k^+ (Fig. 8b).

Compared to the experiments in Fig. 7, the corrected Chien model improves the mass flow, temperature, and Mach number profiles to a certain degree except that the resulting velocity profile shows a little more departure from the data in the outer region than in case 3. From Table 3, the improvement due to the compressibility corrections in predicting δ^* is notable. Including explicit compressibility corrections in standard k–ϵ models, therefore, generally improves the accuracy of the results in the hypersonic nozzle case that we investigated.

Conclusions

A numerical study of the turbulent flow in a M4 supersonic and a M7 hypersonic wind-tunnel nozzle has been performed to verify the influence of turbulence transport, explicit compressibility, and transition location on the computations. On the basis of the results presented here, the following conclusions are appropriate to the types of nozzle flow computations investigated.

1) From the computational point of view, modeling turbulence transport is probably not necessary in supersonic nozzle simulations since the results obtained with the Baldwin–Lomax model, a simple algebraic model, are good enough for engineering applications. When computing the hypersonic wind-tunnel nozzle flow, however, a two-equation turbulence model, i.e., the k–ϵ model of Chien, gives better comparison to the experimental measurements than the Baldwin–Lomax model. The improvements could be due to the transport effects included in the k–ϵ model.

2) For the hypersonic case, modeling the explicit compressibility terms introduces nonnegligible effects into the flowfield, most notably inside the boundary layer. Compared to the experimental data available, including explicit compressibility corrections in standard k–ϵ models has positive effect to improve the accuracy of the hypersonic nozzle simulations. Further studies on this topic would be interesting and necessary.

3) A small variation of the transition location in near throat region has substantial global effects on the computed results downstream, especially on the predicted boundary-layer profiles, displacement thickness, local skin friction coefficient, and Stanton number. Even at the nozzle exit section, the local flow properties obtained are still quite sensitive to this variation.

Acknowledgments

References

[1]Hopkins, E. J., and Keener, E. R., "Pressure-Gradient Effects on Hypersonic Turbulent Skin-Friction and Boundary-Layer Profiles," *AIAA Journal*, Vol. 10, No. 9, 1972, pp. 1141, 1142.

[2]Bushnell, D. M., and Beckwith, I. E., "Calculation of Nonequilibrium Hypersonic Turbulent Boundary Layers and Comparisons with Experimental Data," *AIAA Journal*, Vol. 8, No. 8, 1970, pp. 1462–1469.

[3]Morkovin, M., "Effects of Compressibility on Turbulent Flows," *Mecanique de la Turbulence*, edited by A. Favre, Editors du Centre National de la Recherche Scientifique, Paris, France, 1962, pp. 367–380.

[4]Bradshaw, P., "Compressible Turbulent Shear Layers," *Annual Review of Fluid Mechanics*, Vol. 9, 1977, pp. 33–54.

[5]Bradshaw, P., Launder, B. E., and Lumley, J. L., "Collaborative Testing of Turbulence Models," *Journal of Fluids Engineering*, Vol. 113, March 1991, pp. 3–4.

[6]Nichols, R. H., "A Two-Equation Model for Compressible Flows," AIAA Paper 90-0494, Jan. 1990.

[7]Wilcox, D. C., "Progress in Hypersonic Turbulence Modeling," AIAA Paper 91-1785, June 1991.

[8]Zeman, O., "A New Model for Super/Hypersonic Turbulent Boundary Layers," AIAA Paper 93-0897, Jan. 1993.

[9]Baldwin, B. S., and Lomax, H., "Thin Layer Approximation and Algebraic Model for Separated Turbulent Flow," AIAA Paper 78-257, Jan. 1978.

[10]Chien, K. Y., "Predictions of Channel and Boundary Layer Flows with a Low Reynolds Number Turbulence Model," *AIAA Journal*, Vol. 20, No. 1, 1982, pp. 33–38.

[11]Kim, S. C., and Harloff, G. J., "Hypersonic Turbulent Wall Boundary Layer Computations," Sverdrup Technology Inc., NASP CR 1020, Middleburg Heights, OH, Aug. 1988.

[12]Muylaert, J., Voiron, T., Sagnier, P., Lourme, D., Papirnyk, O., Hannemann, K., Bütefisch, K., and Koppenwallner, G., "Review of the European Hypersonic Wind Tunnel Performance and Simulation Requirements," *Proceedings of the First European Symposium on Aerothermodynamics for Space Vehicles*, European Space Agency, ESA SP-318, Noordwijk, The Netherlands, 1991, pp. 559–574.

[13]Vandromme, D., "Turbulence Modeling for Compressible Flows and Implementation in Navier–Stokes Solvers," *Introduction to the Modeling of Turbulence*, Lecture Notes, von Kármán Inst. for Fluid Dynamics, Brussels, Belgium, March 1991.

[14]Zeman, O., "Dilatation Dissipation: The Concept and Application in Modeling Compressible Mixing Layers," *Physics of Fluids A*, Vol. 2, No. 2, 1990, pp. 178–188.

[15]Sarkar, S., Erlebacher, G., Hussaini, M. Y., and Kreiss, H. O., "The Analysis and Modelling of Dilatational Terms in Compressible Turbulence," *Journal of Fluid Mechanics*, Vol. 227, 1991, pp. 473–493.

[16]Rizzi, A., Eliasson, P., Lindblad, I., Hirsch, C., Lacor, C., and Haeuser, J., "The Engineering of Multiblock/Multigrid Software for Navier–Stokes Flows on Structured Meshes," *Computers and Fluids*, Vol. 22, No. 2/3, 1993, pp. 341–367.

[17]Rizzi, A., and Müller, B., "Large-Scale Viscous Simulation of Laminar Vortex Flow Over a Delta Wing," *AIAA Journal*, Vol. 27, No. 7, 1989, pp. 833–840.

[18]Hu, J. S., and Rizzi, A., "Numerical Investigation of Turbulent Flows in FFA HYP 500 Nozzles," Aeronautical Research Inst. of Sweden, FFA TN 1993-58, Bromma, Sweden, Dec. 1993.

[19]Hovstadius, G., "Measurement of Boundary Layer Properties in Two Hypersonic Nozzles," Aeronautical Research Inst. of Sweden, FFA Rept. AU-624, Stockholm, Sweden, May 1971.

[20]Hovstadius, G., "A Mass-Flow Probe for Measurement in High-Enthalpy Supersonic Boundary Layers," Aeronautical Research Inst. of Sweden, FFA Rept. 128, Stockholm, Sweden, March 1977.

[21]Cebeci, T., and Smith, A. M. O., *Analysis of Turbulent Boundary Layers*, Academic, New York, 1974, pp. 91–103.